GDCh

Research Articles

Angewandte
Chemie
International Edition
www.angewandte.org

Osmotic Energy Harvesting

Thermo-Osmotic Energy Conversion Enabled by Covalent-Organic-Framework Membranes with Record Output Power Density

Xiuhui Zuo, Changjia Zhu, Weipeng Xian, Qing-Wei Meng, Qing Guo, Xincheng Zhu, Sai Wang, Yeqing Wang, Shengqian Ma, and Qi Sun*

Abstract: A vast amount of energy can be extracted from the untapped low-grade heat from sources below 100°C and the Gibbs free energy from salinity gradients. Therefore, a process for simultaneous and direct conversion of these energies into electricity using permselective membranes was developed in this study. These membranes screen charges of ion flux driven by the combined salinity and temperature gradients to achieve thermo-osmotic energy conversion. Increasing the charge density in the pore channels enhanced the permselectivity and ion conductance, leading to a larger osmotic voltage and current. A 14-fold increase in power density was achieved by adjusting the ionic site population of covalent organic framework (COF) membranes. The optimal COF membrane was operated under simulated estuary conditions at a temperature difference of 60 K, which yielded a power density of $\approx 231 \text{ W m}^{-2}$, placing it among the best performing upscaled membranes. The developed system can pave the way to the utilization of the enormous supply of untapped osmotic power and low-grade heat energy, indicating the tremendous potential of using COF membranes for energy conversion applications.

Introduction

Low-grade heat ($< 100°C$) produced from industrial processes to living organisms is ubiquitous. Over 30% of the global primary energy consumption has been estimated to be dissipated in the form of this low-grade heat.[1] However,

[*] X. Zuo, W. Xian, Q.-W. Meng, Q. Guo, X. Zhu, Dr. S. Wang, Prof. Q. Sun
Zhejiang Provincial Key Laboratory of Advanced Chemical Engineering Manufacture Technology, College of Chemical and Biological Engineering, Zhejiang University
Hangzhou, 310027 (China)
E-mail: sunqichs@zju.edu.cn

C. Zhu, Prof. S. Ma
Department of Chemistry,
University of North Texas
1508 W Mulberry St Denton, TX 76201 (USA)

Dr. Y. Wang
Key Lab of Applied Chemistry of Zhejiang Province
Department of Chemistry
Zhejiang University, Hangzhou 310028 (China)

this type of energy has yet to be efficiently utilized despite its abundance. In parallel, a vast amount of energy can be derived from the salinity gradient between solutions, based on their chemical potential differences.[2] The utilization of these energy sources has attracted increasing attention for mitigating the energy crisis and enabling carbon emission reduction. Recent theoretical developments in nanofluidics have established a connection between the potential, solution activity, and temperature at the interphase of a membrane, which can be expressed using Equation (1), in which V_{oc} is the open-circuit voltage; γ_{low} and γ_{high}, c_{low} and c_{high}, and T_{low} and T_{high} are the activity coefficients, concentrations, and temperatures of the low concentration and high concentration solutions, respectively; and R, t_+, and F are the gas constant, cation transference number, and Faraday constant, respectively.[3] This equation establishes the basis for the simultaneous conversion of osmotic power and low-grade heat energy into electricity.

$$V_{oc} = -2t_+ \left(\frac{RT_{low}}{F} \ln\gamma_{low}c_{low} - \frac{RT_{high}}{F} \ln\gamma_{high}c_{high} \right) \quad (1)$$

Given that the output power density is proportional to the potential and internal conductance, the efficacy of a pertinent energy conversion device is contingent on the ability of ion-selective membranes to facilitate directional charge transport and on the membrane resistance for ion transmission. Despite significant differences in various types of materials, membrane-based separation processes primarily depend on the control of host-guest interactions in a confined geometry. The electrostatic forces arising from the charged sites on the pore channels lay the foundation for numerous ion separation processes; these forces are particularly crucial interactions owing to the significant influence of electrostatics on the ion transport at length scales several times the ion size.[4] Therefore, tremendous efforts have been directed toward the manipulation of the charge population at the nanoscale to elucidate the fundamental ion transport behavior across the charged channels of nanoporous membranes.[5]

Reticular materials, such as covalent organic frameworks (COFs), enable the association of discrete struts into designed structures, providing an opportunity to investigate the role of charge density.[6] When a target topology is envisioned, the molecular units are amenable to direct assembly, thus permitting the regulation of the ionic site population in the same pore structure.[7] The effects of charge density on ion permselectivity and transmembrane

resistance were comprehensively investigated in the present study by leveraging the multivariate (MTV) strategy. Our previous research revealed a volcano-like curve by plotting the membrane charge density versus the output power density when optimizing the content of cationic sites in anion-selective membranes. To form a complete RED battery, anion-selective membranes should be used in conjunction with a cation-selective membrane to facilitate the directional permeation of ions. Therefore, establishing the connection between the density of anionic groups and output power efficiency is essential to achieving an efficient RED device. In this study, we found that contradicted with the anion-selective membranes, a higher charge density in the cation-selective membrane enables stronger repulsion of co-ions and quicker counter-ion passage, thus enhancing permselectivity and reducing the counter-ion transport barrier (Figure 1). The optimal membrane in contact with 0.5 M and 0.01 M NaCl solutions afforded an output power density of up to 97 W m^{-2}, which increased to 231 W m^{-2} after the introduction of a temperature gradient of 60 K, a value that is approximately 46-fold higher than the commercial benchmark for osmotic energy harvesting (≈ 5 W m^{-2}).[2e]
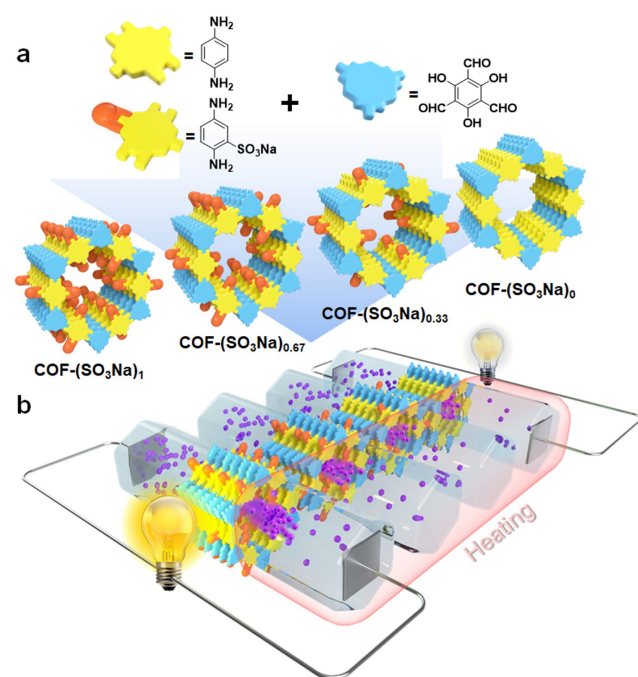
Figure 1. a) Synthetic scheme of ionic covalent-organic-framework (COF) membranes with varied charge density and b) conceptual illustration of the conversion of energies derived from low-grade heat and salinity differences into electricity using ionic COF membranes, and the impact of the membrane charge density on the output power density.

Results and Discussion

Membrane synthesis was initiated by the condensation of triformylphloroglucinol (Tp) and diamine compounds with and without sulfonate groups as substituents, namely sodium 2,5-diaminobenzenesulfonate and benzene-1,4-diamine. The diamine compounds and Tp were dissolved in an aqueous acetic solution and toluene to yield the aqueous and organic phases, respectively, which were transferred into a vessel with two chambers segregated by a polyacrylonitrile (PAN) ultrafiltration membrane (Figure S1). COF active layers were grown on the PAN membrane to enhance the operational stability. The vessel was maintained at 70°C in an oven for 3 d and was subsequently removed. The membrane was removed from the vessel and washed sequentially with ethanol and water, revealing a vermeil film on the PAN surface. Varying the initial diamine compound ratios under the aforementioned membrane growth conditions provided control of the charge density of the resulting membranes, which are denoted as COF-(SO$_3$Na)$_x$/PAN, where x refers to the initial molar ratio of sodium 2,5-diaminobenzenesulfonate to the diamine compounds (Figure S2). The membranes were characterized by Fourier transform infrared (FTIR) spectroscopy, which revealed the attenuation of the primary amine stretch region (–NH$_2$; 3303–3330 cm^{-1}) and the appearance of a new C–N stretch at 1283 cm^{-1}, which is characteristic of β-ketoenamine bonds.[8] The disappearance of the –NH$_2$ absorption from the diamine compounds and aldehyde (–C=O; 1643 cm^{-1}) indicates a high degree of polymerization of the membranes. Vibration bands associated with O=S=O stretching bonds (1082 cm^{-1} and 1028 cm^{-1}) appeared,[9] and their relative intensities increased with increasing values of x, indicating the preservation of sulfonate groups during the condensation (Figure S3). The signal at 184.2 ppm in the solid-state ^{13}C nuclear magnetic resonance (^{13}C NMR) spectra ppm corresponds to the keto form of carbonyl carbon, further manifesting the target chemical structure (Figure S4). The measured static contact angles of water on the COF-(SO$_3$Na)$_x$/PAN membranes (72°–19°) decreased as x increased from 0 to 1 (Figure S5). The enhancement in membrane hydrophilicity can facilitate contact with water and consequently promote transmembrane ion migration. The elemental distribution mappings collected using an electron microprobe analyzer (EMPA) revealed the homogeneous distribution of S species throughout the membranes, with estimated contents of 10, 3.1, and 0.8 wt % for COF-(SO$_3$Na)$_1$/PAN, COF-(SO$_3$Na)$_{0.67}$/PAN, and COF-(SO$_3$Na)$_{0.33}$/PAN, respectively (Figure S6 and Table S1). The positive correlation between the stoichiometry of the starting monomers and the actual moiety ratios in the obtained COF membranes validated the aforementioned characterization results. The zeta potentials of the COF-(SO$_3$Na)$_x$/PAN membranes become more negative with increasing in x values (Table S2). The X-ray diffraction (XRD) patterns of free-standing COF-(SO$_3$Na)$_x$ membranes showed a set of diffraction peaks at approximately 4.7°, 8.3°, and 27.0°, indicating high crystallinity of the membranes (Figure 2a). N$_2$ sorption isotherms were acquired at 77 K to

Angew. Chem. Int. Ed. **2022**, 61, e202116910 (2 of 8)

© 2022 Wiley-VCH GmbH
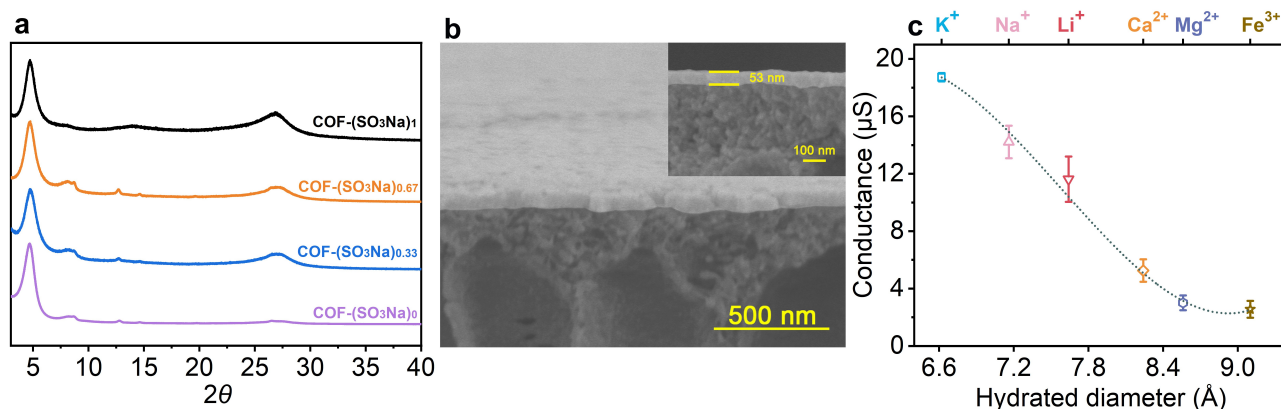
Figure 2. a) XRD patterns of the free-standing COF membranes. b) Cross-sectional SEM image of COF-$(SO_3Na)_1$/PAN. Inset shows the high magnification cross-sectional image. c) Ion conductance of various electrolytes (0.1 M) in contact with COF-$(SO_3Na)_1$/PAN. Cations and their corresponding hydrated diameters are shown on the top and bottom x-axes, respectively.

estimate the porosity and pore size distribution of the COF-based membranes via Brunauer–Emmett–Teller (BET) surface area analysis and the nonlocal density functional theory (NLDFT), respectively. The BET surface areas and pore sizes of the resulting membranes decrease in the order of COF-$(SO_3Na)_0$ > COF-$(SO_3Na)_{0.33}$ > COF-$(SO_3Na)_{0.67}$ > COF-$(SO_3Na)_1$. The estimated accessible pore size of the free-standing COF-$(SO_3Na)_x$ membrane (≈ 1.4–1.8 nm) was consistent with that of the staggered AA stacking model (Figures S7 and S8). The microporous channels enable overlap of the electrical double layers (EDLs) of a wide range of ionic strengths, resulting in high selectivity and membrane potentials with high magnitudes (Table S3). Scanning electron microscopy (SEM) images revealed continuous and crack-free COF surfaces that contoured the PAN support with a thickness of ≈ 53–65 nm (Figure 2b and Figures S9–S13). Notably, the thickness of the COF active layer can be readily adjusted by varying the concentrations of the monomers (Figure S14). The compactness of the COF-$(SO_3Na)_x$/PAN membranes was examined by evaluating their performance in the rejection of mono- and multivalent salts (NaCl and $MgSO_4$), which revealed an almost complete rejection of $MgSO_4$ and the transmission of NaCl (Figure S15). The full rejection of $MgSO_4$ can be rationalized by the Donnan's membrane equilibrium model.[10] The integrity of the membrane was further confirmed by measuring the conductance of the membrane in contact with various ions, which showed a decreasing trend with an increase in the hydration radius (Figure 2c). Considering that the pore size of the COF channel is larger than the tested hydrated ion diameters, the molecular sieving effect cannot be used to explain the conductivity trend. It is well-studied that hydrolytic sulfonate ligand exhibits greater affinity towards ions that are more hydratable, increasing in the order of Fe^{3+} > Mg^{2+} > Ca^{2+} > Li^+ > Na^+ > K^+. Lower binding affinity leads to a more difficult condensation of the cation-sulfonate pairs, and hence easier for dissociation for surface jumping and fast transportation.[4b]

Upon the realization of membranes with various charge populations, the impact of the ionic density of COF-$(SO_3Na)_x$/PAN on the ion transport properties across the membranes was first investigated to validate the confinement effects and the surface-charge-governed ion transport behavior. To this end, a membrane was inserted between two half-cells of a symmetric H-type electrochemical cell, which contained aqueous KCl solutions of identical concentrations, and the circuit was completed with a pair of Ag/AgCl electrodes immersed in each half-cell (Figure 3a, inset). KCl was selected because of the comparable diffusion coefficients of K^+ and Cl^- ions ($\approx 1.96 \times 10^{-9}$ $m^2 s^{-1}$ and $\approx 2.03 \times 10^{-9}$ $m^2 s^{-1}$, respectively), which enabled the minimization of the liquid junction potentials.[11] Figure 3a and Figure S16 show the ionic–current–voltage (I–V) curves recorded using KCl solutions with concentrations ranging from 0.01 mM to 3 M, which revealed a linear ohmic behavior. Therefore, the transmembrane ion conductance can be derived from the slopes of these curves. The plots of ionic conductivity versus KCl concentration revealed that the conductivities of COF-$(SO_3Na)_x$/PAN deviated from the bulk behavior (proportional to the concentration; dashed line) at ≈ 0.1 M and gradually plateaued at lower concentrations, exceeding the bulk values by orders of magnitude (Table S3). Notably, the resulting conductivities considerably deviated from the bulk value with an increase in the charge population of the membranes (Figure 3b). These phenomena can be explained using the excess of oppositely charged ions that are attracted upon contact between a charged surface and an electrolyte solution, which induces EDL formation and yields the enhanced conductivity compared to that of the bulk electrolyte. Moreover, ion diffusion through the membrane is drastically affected by electrostatic interactions when the EDLs overlap in the pore channels, which clarifies the transport of counter-ions.[12]

Given that the potential and current are derived only from charge separation, ion selectivity is crucial for realizing the thermal-osmotic energy conversion into electricity. To quantitatively evaluate the impact of charge density on
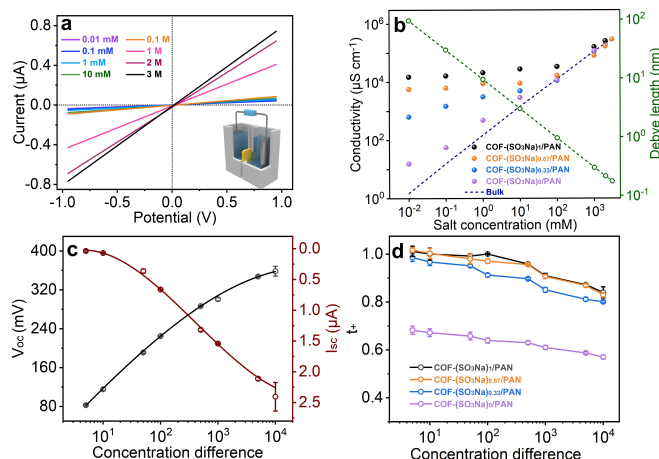
Figure 3. a) *I–V* curves for COF-(SO$_3$Na)$_1$/PAN recorded using KCl solutions with concentrations ranging from 0.01 mM to 3 M. Inset: schematic of setup used for the investigation of ion transport behavior across the fabricated membranes. b) Ion conductivity of COF-(SO$_3$Na)$_x$/PAN and Debye length versus KCl concentration. When the KCl concentration is below 0.1 M, the channel size of COF-(SO$_3$Na)$_x$ is smaller than the Debye length (olive dashed line), leading to the overlap of the EDLs and a deviation in ion conductivity from the bulk value. c) Plots of the recorded *V*$_{oc}$ and *I*$_{sc}$ versus differences in KCl concentration across COF-(SO$_3$Na)$_1$/PAN, and (d) plots of transference number (*t*$_+$) versus differences in KCl concentration across COF-(SO$_3$Na)$_x$/PAN. The KCl concentration of the PAN-facing cell (low concentration side) was set to 0.1 mM. Error bars represent the standard deviation of three individual measurements.

membrane permselectivity, *I–V* curves were collected using a wide range of KCl concentration differences across the COF-(SO$_3$Na)$_x$/PAN membranes. The KCl concentration of the cell in contact with PAN was fixed at 0.1 mM, whereas that of the cell facing the COF active layer increased from 0.5 mM to 1 M. Plots of *V*$_{oc}$ and short-circuit current (*I*$_{sc}$) versus concentration differences for COF-(SO$_3$Na)$_x$/PAN are shown in Figure 3c and Figure S17. The permeability was determined by estimating the *t*$_+$ values for various salinity differences using Equation (1). The surface charge distribution was found to considerably affect the ion screening performance of the membranes. COF-(SO$_3$Na)$_0$/PAN showed a negligible ion screening ability, yielding *t*$_+$ values close to 0.6 at concentration differences in the range of 10^2–10^4. The slight cation transport selectivity can be rationalized based on the charge distribution along the pores calculated using the quantum density functional theory (Figure S18). The negative partial charge of the oxygen species facilitated cation transport. The incorporation of sodium benzenesulfonate moieties remarkably improved the permselectivity. COF-(SO$_3$Na)$_{0.33}$/PAN with an ionic site content of 0.25 mmol g^{-1} exhibited a significantly increased permselectivity, achieving a *t*$_+$ value of 0.8 even at a concentration difference of 10^4. Increasing the content of the sodium benzenesulfonate moieties from 0.25 mmol g^{-1} to 3.18 mmol g^{-1} resulted in a gradual improvement in permselectivity with increasing charge population (Figure 3d).

The high ion selectivity of COF-(SO$_3$Na)$_x$/PAN prompted an investigation of their performance in reverse electrodialysis (RED) for osmotic energy extraction by loading an external resistor (*R*$_L$) to export the generated power. Aqueous NaCl solutions (0.01/0.5 M) were employed to mimic estuary conditions, and two configurations were established by manipulating the orientation of the membranes to optimize the RED device efficiency. A higher value was achieved by the arrangement featuring the COF layers facing the low-concentration side (Figure S19), which was attributed to the suppressed concentration polarization. All the investigated membranes showed a similar trend involving a gradual decrease in the osmotic current with increasing *R*$_L$. Moreover, the output power density peaked at *R*$_L$ values of 8.2, 9.9, 14.2, and 29.3 kΩ for COF-(SO$_3$Na)$_1$/PAN, COF-(SO$_3$Na)$_{0.67}$/PAN, COF-(SO$_3$Na)$_{0.33}$/PAN, and COF-(SO$_3$Na)$_0$/PAN, respectively (Figure 4a and Figure S20). The RED device is known to achieve maximum output power density when *R*$_L$ is equal to the membrane internal resistance, thus implying that the resistance of the COF-(SO$_3$Na)$_x$/PAN membranes decrease as the charge population increases.[2f] Indeed, the energy barrier of Na$^+$-ion transport was calculated to be 34.9 kJ mol^{-1} and 15.6 kJ mol^{-1} for COF-(SO$_3$Na)$_0$/PAN and COF-(SO$_3$Na)$_1$/PAN, respectively, indicating improved ion transport at a higher charge density (Figure 4b). Notably, the estimated internal resistance of COF-(SO$_3$Na)$_1$/PAN (8.2 kΩ) is one of the lowest values reported for RED membranes (Table S4). The power density was calculated using the equation, $P_{out} = \frac{I_{sc}V_{oc}}{4S}$, to be 97, 63, 44, and 7 W m^{-2} for COF-(SO$_3$Na)$_1$/PAN, COF-(SO$_3$Na)$_{0.67}$/PAN, COF-(SO$_3$Na)$_{0.33}$/PAN, and COF-(SO$_3$Na)$_0$/PAN, respectively [Eqs. (S7) and (S8)]. The value for COF-(SO$_3$Na)$_1$/PAN, in particular, is approximately 20-fold higher than the commercial benchmark. COF-(SO$_3$Na)$_1$ with the lowest BET surface area among the membranes evaluated, afforded the highest output power density, highlighting the role of charge density. We therefore ascribe the ultrahigh osmotic energy conversion efficiency of COF-(SO$_3$Na)$_1$/PAN to its high ionic density and low membrane thickness (Figure S21). To confirm the efficiency of the RED battery, we assembled 11 electrochemical cells, each of which was segregated by COF-(SO$_3$Na)$_1$/PAN and alternatively filled with 0.01 and 0.5 M NaCl aqueous solutions. The resulting device can directly power a calculator (see details in Figure S22). Moreover, the RED device constructed using COF-SO$_3$Na$_1$/PAN afforded a *V*$_{oc}$ of 162.9 mV, which corresponds to an energy conversion efficiency of 42%, placing it among the most efficient RED systems developed to date (Table S4). It is noteworthy that the measured *V*$_{oc}$ actually consists of two parts: the diffusion potential (*Φ*$_{diff}$) which is contributed by the selective ion transport and the redox potential (*Φ*$_{redox}$) which is generated by the unequal potential drop at the electrode-solution interface. The generated power density as a result of selective ion diffusion was calculated to be 29, 16, 9, and 0.05 W m^{-2} for COF-(SO$_3$Na)$_1$/PAN, COF-(SO$_3$Na)$_{0.67}$/PAN, COF-(SO$_3$Na)$_{0.33}$/PAN, and COF-(SO$_3$Na)$_0$/PAN, respectively (Table S5).
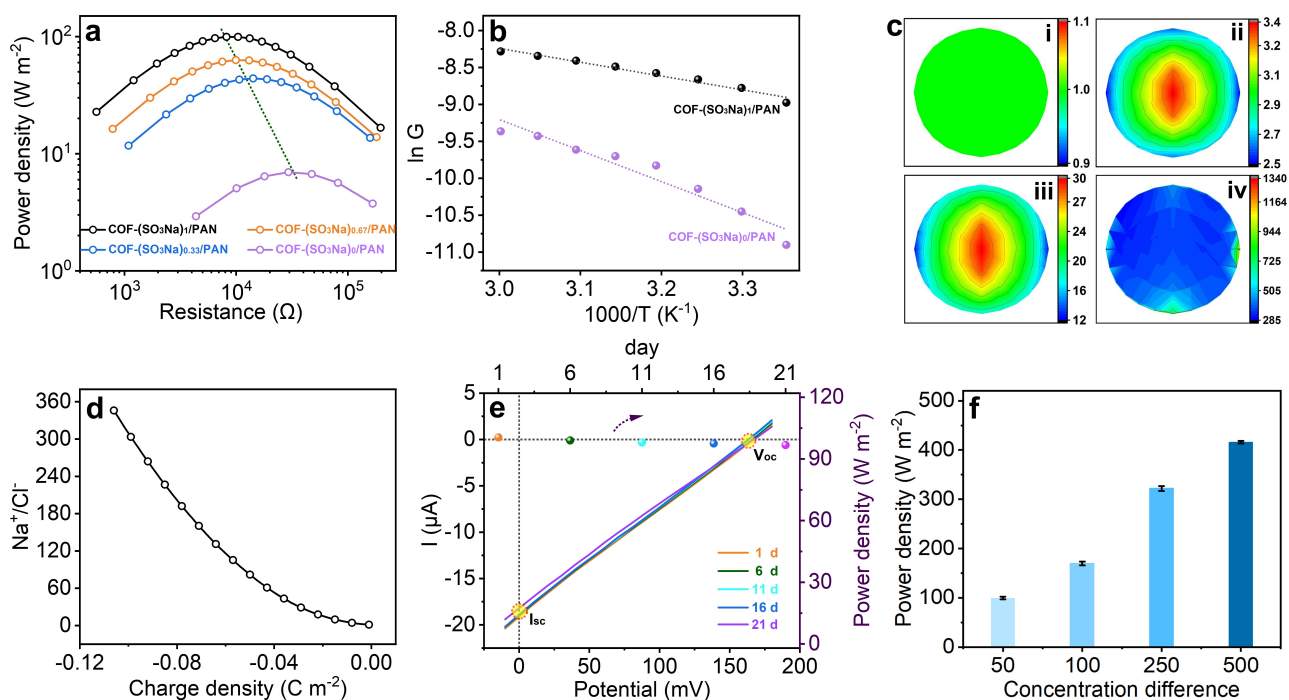
Figure 4. a) Generated power outputted to an external circuit using an external resistor (R_L) under a NaCl concentration difference of 0.01 /0.5 M over COF-(SO$_3$Na)$_x$/PAN. b) Ion conductance curves versus temperature across COF-(SO$_3$Na)$_x$/PAN and the corresponding Arrhenius plot. c) The x-y cross-sectional concentration images of the ratio of Na$^+$/Cl$^-$ taken at 0 nm along the z-axis (i.e. at the mouth of the low concentration side). i) COF-(SO$_3$Na)$_0$/PAN, ii) COF-(SO$_3$Na)$_{0.33}$/PAN, iii) COF-(SO$_3$Na)$_{0.67}$/PAN, and iv) COF-(SO$_3$Na)$_1$/PAN. d) Plots of the Na$^+$/Cl$^-$ ratio at the circle center derived from (c). e) Time evolutions of the V_{oc}, I_{sc}, and output power density of the COF-(SO$_3$Na)$_1$/PAN-based RED device in 0.01/0.5 M NaCl concentration difference. f) Maximum extractable energy obtained by mixing saline solutions with various concentration differences, in which the NaCl concentrations in the low-and high-concentration sides was maintained at 0.01 M and was increased from 0.5 M to 5 M, respectively.

To enable a molecular-level understanding of the effects of charge density, the ion distributions along the channels with varied charge densities were investigated using COMSOL Multiphysics software. Three-dimensional models with a channel of 53 nm in length and 1.4 nm in diameter, and two separated cells with a volume of 1.2×10^4 nm^3 were constructed to facilitate the calculation (according to the membrane thickness and the COF pore size, respectively; Figure S23). Given that the electric signals generated under a concentration gradient originate from the cation selectivity, the ratio of Na$^+$/Cl$^-$ was plotted against the surface charge density at the mouth of the low-concentration side. The Na$^+$/Cl$^-$ ratio increased with an increase in the aforementioned surface charge density, suggesting that a higher charge density of the nanochannels could facilitate charge screening and yield a high osmotic potential and net diffusion current (Figures 4c, d, and S24).

The COF-(SO$_3$Na)$_1$/PAN membranes were used in the subsequent experiments owing to their superior performance. First, the long-term stability of the COF-(SO$_3$Na)$_1$/PAN-based device, which is a critical parameter for practical applications, was evaluated by soaking the membranes in 0.01/0.5 M NaCl gradient cells for 21 d and monitoring the osmotic voltage and current daily. Negligible attenuation was observed during this experiment, validating the durability of COF-(SO$_3$Na)$_1$/PAN (Figure 4e and Figure S25). The

retention of structural crystallinity enables long-term power production, thus aiding the proliferation of osmotic energy plants (Figure S26). In addition to the salinity gradients in estuaries, brine from desalination plants can be a promising source. The output power density increased with increasing differences in salinity, affording a value of 416 W m^{-2} at a 500-fold difference in salinity (Figure 4f). The decreased ion transmembrane barrier with increasing in salinity gradient, which leads to a large osmotic current, can be used to rationalize the boosted output power density at a high salinity difference (Figure S27).

In parallel, an enormous amount of waste heat, accounting for 20–70 % of the total energy consumption, is discharged from industrial plants; this is an environmental issue and contributes to an increase in energy costs.[1] Therefore, waste heat-energy recovery is attracting increasing attention, especially for recovering low-grade heat. To this end, the design of salinity gradient heat engines has been focused on because of their potential cost-effectiveness and the flexibility for direct conversion of the heat and the salinity gradient into electricity. According to Equation (1), temperature differences between the electrolytes can not only lead to a remarkable transmembrane potential but also increase the ion conductance by increasing the ion mobility. Indeed, the ion conductance of COF-(SO$_3$Na)$_1$/PAN exhibited a linear relationship with temperature and followed the
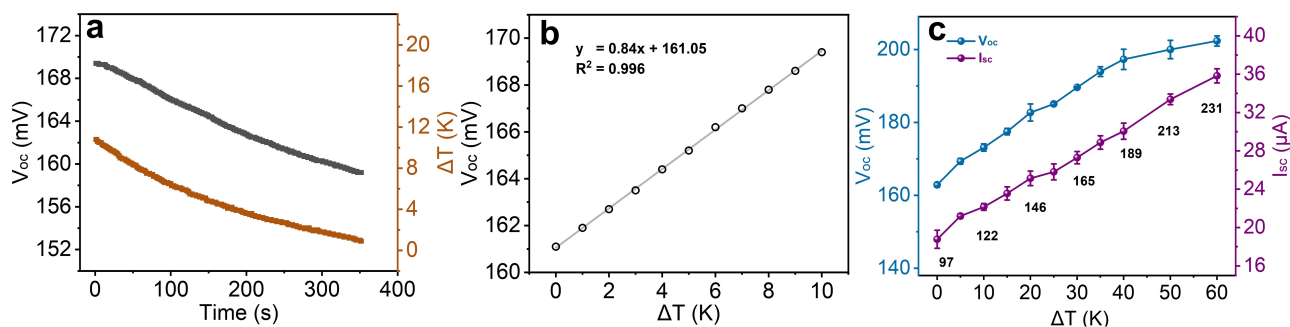
Figure 5. a) Synchronous time evolution of ΔV_{oc} in response to the temperature changes of 0.01 M NaCl. b) Linear fits of $\Delta V_{oc} - \Delta T$ plots to evaluate the thermosensation sensitivity; R^2 values greater than 0.99 were obtained. c) Variations in V_{oc} and I_{sc}, and the corresponding output power density (black numbers) of COF-$(SO_3Na)_1$/PAN in response to the imposed temperature gradients. The temperature of the low temperature side is set as 293 K.

Arrhenius law, confirming that an increase in the electrolyte temperature facilitated transmembrane ion transport. Consequently, the imposition of a temperature gradient on the RED device was expected to increase both the osmotic potential and current, with an accompanying increase in output power density.

Given that the ions spontaneously move from the low- to high-temperature sides, according to the principle of increasing entropy, the dilute solution was warmed using a heat rod to introduce a temperature gradient to ensure that the heat-driven ion transport was in the same direction as that of the salinity gradient (Figures S28 and S29). The thermoelectric conversion efficiency was quantitatively determined by measuring the instantaneous temperature gradients of the electrolyte solutions (ΔT), I_{sc}, and V_{oc}. The temperature differences between the electrolyte solutions in the two half-cells were controlled within 10 K to eliminate the influence of temperature variation on the electrode potential. Figure 5a shows that V_{oc} and ΔT vary synchronously with time in 0.01/0.5 M NaCl concentration gradient. Plotting ΔV_{oc} against ΔT resulted in a linear relationship, and the corresponding slope, which represented thermosensation selectivity, was estimated to be 0.84 mV K^{-1} (Figure 5b). Accordingly, V_{oc} and I_{sc} increased by 8.4 mV and 5.7 µA at $\Delta T = 10$ K. The efficiency of the thermo-osmotic energy conversion increased from 97 W m^{-2} to 132 W m^{-2} (an enhancement of 36.1%) upon increasing the temperature of the 0.01 M NaCl solution by 10 K. A further increase in the imposed temperature gradient to 60 K led to an output power density of 231 W m^{-2}, which was double that achieved without the temperature gradient (Figure 5c). The increased voltage and current with increasing in temperature differences, resulting in the considerably enhanced power generation efficiency. Moreover, the corresponding internal resistance decreased by approximately 31.7% (from 8.2 kΩ to 5.6 kΩ, Figure S30). Notably, similar trajectories were observed for the time evolution of V_{oc} and ΔT over a wide range of salinity gradients, offering thermosensation selectivity of 0.84 and 0.81 mV K^{-1} in 0.01/0.1 M and 0.01/1 M NaCl gradients, respectively (Figures S31 and S32), thus showing application prospects in various systems. In addi-

tion, negligible attenuation in terms of V_{oc}, I_{sc}, and output power density of COF-$(SO_3Na)_1$/PAN were observed after being treated with boiling water for 8 h, validating its thermal stability (Figure S33).

Conclusion

The use of a COF-based ion-selective membrane for harvesting energy from low-grade heat sources and the inherent Gibbs free energies of fluid systems was demonstrated. The effects of the charge population on the ion permselectivity and conductance across the isostructural COF-based membranes were probed. In addition to enabling higher ion selectivity, we found that within the range of charge density investigated herein, a higher charge population resulted in a lower barrier to ion transmembrane transport. The maximum output power density reached 97 W m^{-2} under estuary-mimicking conditions, which is approximately 20-fold that of the commercialization benchmark. The power value can be further boosted by imposing a temperature gradient, reaching 231 W m^{-2} for the optimal-membrane-based device in the presence of a temperature difference of 60 K. These findings are anticipated to facilitate the development of promising energy conversion systems for large-scale sustainable energy harvesting and for powering small-scale devices.

Conflict of Interest

The authors declare no conflict of interest.

Angew. Chem. Int. Ed. **2022**, *61*, e202116910 (6 of 8)

© 2022 Wiley-VCH GmbH

Data Availability Statement

The data that support the findings of this study are available from the corresponding author upon reasonable request.

[1] a) D. Lindley, *Nature* **2009**, *458*, 138–141; b) J. Duan, B. Yu, L. Huang, B. Hu, M. Xu, G. Feng, J. Zhou, *Joule* **2021**, *5*, 768–779; c) A. P. Straub, N. Y. Yip, S. Lin, J. Lee, M. Elimelech, *Nat. Energy* **2016**, *1*, 16090; d) S. W. Lee, Y. Yang, H.-W. Lee, H. Ghasemi, D. Kraemer, G. Chen, Y. Cui, *Nat. Commun.* **2014**, *5*, 3942; e) G. Xie, P. Li, Z. Zhang, K. Xiao, X.-Y. Kong, L. Wen, L. Jiang, *Adv. Energy Mater.* **2018**, *8*, 1800459; f) W. Zhou, K. Yamamoto, A. Miura, R. Lguchi, Y. Miura, K.-i. Uchida, Y. Sakuraba, *Nat. Mater.* **2021**, *20*, 463–467; g) T. Li, X. Zhang, S. D. Lacey, R. Mi, X. Zhao, F. Jiang, J. Song, Z. Liu, G. Chen, J. Dai, Y. Yao, S. Das, R. Yang, R. M. Briber, L. Hu, *Nat. Mater.* **2019**, *18*, 608–613; h) A. P. Straub, M. Elimelech, *Environ. Sci. Technol.* **2017**, *51*, 12925–12937; i) K. Chen, L. Yao, F. Yan, S. Liu, R. Yang, B. Su, *J. Mater. Chem. A* **2019**, *7*, 25258–25261; j) P. Catrini, A. Cipollina, G. Micale, A. Piacentino, A. Tamburini, *Energy Convers. Manage.* **2021**, *237*, 114135; k) P. Palenzuela, M. Micari, B. Ortega-Delgado, F. Giacalone, G. Zaragoza, D.-C. Alarcón-Padilla, A. Cipollina, A. Tamburini, G. Micale, *Energy* **2018**, *11*, 3385; l) C. Wu, T. Xiao, J. Tang, Q. Zhang, Z. Liu, J. Liu, H. Wang, *Nano Energy* **2020**, *76*, 105113.

[2] a) Z. Man, J. Safaei, Z. Zhang, Y. Wang, D. Zhou, P. Li, X. Zhang, L. Jiang, G. Wang, *J. Am. Chem. Soc.* **2021**, *143*, 16206–16216; b) Y. Zhu, K. Zhan, X. Hou, *ACS Nano* **2018**, *12*, 908–911; c) G. Z. Ramon, B. J. Feinberg, E. M. V. Hoek, *Energy Environ. Sci.* **2011**, *4*, 4423–4434; d) T. Kim, M. Rahimi, B. E. Logan, C. A. Gorski, *Environ. Sci. Technol.* **2016**, *50*, 9791–9797; e) Z. Zhang, L. Wen, L. Jiang, *Nat. Rev. Mater.* **2021**, *6*, 622–639; f) S. Chen, C. Zhu, W. Xian, X. Liu, X. Liu, Q. Zhang, S. Ma, Q. Sun, *J. Am. Chem. Soc.* **2021**, *143*, 9415–9422; g) L. Ding, D. Xiao, Z. Lu, J. Deng, Y. Wei, J. Caro, H. Wang, *Angew. Chem. Int. Ed.* **2020**, *59*, 8720–8726; *Angew. Chem.* **2020**, *132*, 8798–8804; h) B. E. Logan, M. Elimelech, *Nature* **2012**, *488*, 313–319; i) X. Liu, M. He, D. Calvani, H. Qi, K. B. S. S. Gupta, H. J. M. de Groot, G. J. A. Sevink, F. Buda, U. Kaiser, G. F. Schneider, *Nat. Nanotechnol.* **2020**, *15*, 307–312; j) K. Xiao, P. Giusto, L. Wen, L. Jiang, M. Antonietti, *Angew. Chem. Int. Ed.* **2018**, *57*, 10123–10126; *Angew. Chem.* **2018**, *130*, 10280–10283; k) Y. Xu, Y. Song, F. Xu, *Nano Energy* **2021**, *79*, 105468; l) Z. Zhang, W. Shen, L. Lin, M. Wang, N. Li, Z. Zheng, F. Liu, L. Cao, *Adv. Sci.* **2020**, *7*, 2000286; m) J. Feng, M. Graf, K. Liu, D. Ovchinnikov, D. Dumcenco, M. Heiranian, V. Nandigana, N. R. Aluru, A. Kis, A. Radenovic, *Nature* **2016**, *536*, 197–200; n) A. Siria, P. Poncharal, A.-L. Biance, R. Fulcrand, X. Blase, S. T. Purcell, L. Bocquet, *Nature* **2013**, *494*, 455–458; o) C. Chen, D. Liu, L. He, S. Qin, J. Wang, J. M. Razal, N. A. Kotov, W. Lei, *Joule* **2020**, *4*, 247–261; p) C.-Y. Lin, C. Combs, Y.-S. Su, L.-H. Yeh, Z. S. Siwy, *J. Am. Chem. Soc.* **2019**, *141*, 3691–3698; q) L. Xie, S. Zhou, J. Liu, B. Qiu, T. Liu, Q. Liang, X. Zheng, B. Li, J. Zeng, M. Yan, Y. He, X. Zhang, H. Zeng, D. Ma, P. Chen, K. Liang, L. Jiang, Y. Wang, D. Zhao, B. Kong, *J. Am. Chem. Soc.* **2021**, *143*, 6922–6932; r) Y.-C. Liu, L. H. Yeh, M.-J. Zheng, K. C.-W. Wu, *Sci. Adv.* **2021**, *7*, eabe9924; s) G. Yang, D. Liu, C. Chen, Y. Qian, Y. Su, S. Qin, L. Zhang, X. Wang, L. Sun, W. Lei, *ACS Nano* **2021**, *15*, 6594–6603; t) C. Chen, D. Liu, G. Yang, J. Wang, L. Wang, W. Lei, *Adv. Energy Mater.* **2020**, *10*, 1904098.

[3] a) W. Xian, P. Zhang, C. Zhu, X. Zuo, S. Ma, Q. Sun, *CCS* **2021**, *3*, 2464–2472; b) P. Zhang, S. Chen, C. Zhu, L. Hou, W. Xian, X. Zuo, Q. Zhang, L. Zhang, S. Ma, Q. Sun, *Nat. Commun.* **2021**, *12*, 1844.

[4] a) Y.-M. Tu, W. Song, T. Ren, Y.-X. Shen, R. Chowdhury, P. Rajapaksha, T. E. Culp, L. Samineni, C. Lang, A. Thokkadam, D. Carson, Y. Dai, A. Mukthar, M. Zhang, A. Parshin, J. N. Sloand, S. H. Medina, M. Grzelakowski, D. Bhattacharya, W. A. Phillip, E. D. Gomez, R. J. Hickey, Y. Wei, M. Kumar, *Nat. Mater.* **2020**, *19*, 347–354; b) Y. Guo, Y. Ying, Y. Mao, X. Peng, B. Chen, *Angew. Chem. Int. Ed.* **2016**, *55*, 15120–15124; *Angew. Chem.* **2016**, *128*, 15344–15348; c) R. Tan, A. Wang, R. Malpass-Evans, R. Williams, E. W. Zhao, T. Liu, C. Ye, X. Zhou, B. P. Darwich, Z. Fan, L. Turcani, E. Jackson, L. Chen, S. Y. Chong, T. Li, K. E. Jelfs, A. I. Cooper, N. P. Brandon, C. P. Grey, N. B. McKeown, Q. Song, *Nat. Mater.* **2020**, *19*, 195–202; d) M. A. Shehzad, Y. Wang, A. Yasmin, X. Ge, Y. He, X. Liang, Y. Zhu, M. Hu, X. Xiao, L. Ge, C. Jiang, Z. Yang, M. D. Guiver, L. Wu, T. Xu, *Angew. Chem. Int. Ed.* **2019**, *58*, 12646–12654; *Angew. Chem.* **2019**, *131*, 12776–12784; e) M. Zhang, K. Guan, Y. Ji, G. Liu, W. Jin, N. Xu, *Nat. Commun.* **2019**, *10*, 1253; f) J. Lu, H. Zhang, J. Hou, X. Li, X. Hu, Y. Hu, C. D. Easton, Q. Li, C. Sun, A. W. Thornton, M. R. Hill, X. Zhang, G. Jiang, J. Z. Liu, A. J. Hill, B. D. Freeman, L. Jiang, H. Wang, *Nat. Mater.* **2020**, *19*, 767–774; g) M. Tagliazucchi, O. Peleg, M. Kröger, Y. Rabin, I. Szleifer, *Proc. Natl. Acad. Sci. USA* **2013**, *110*, 3363–3368; h) A. Razmjou, M. Asadnia, E. Hosseini, A. H. Korayem, V. Chen, *Nat. Commun.* **2019**, *10*, 5793.

[5] a) L. Wang, Z. Wang, S. K. Patel, S. Lin, M. Elimelech, *ACS Nano* **2021**, *15*, 4093–4107; b) X. Zhu, J. Hao, B. Bao, Y. Zhou, H. Zhang, J. Pang, Z. Jiang, *Sci. Adv.* **2018**, *4*, eaau1665; c) J. Gao, X. Liu, Y. Jiang, L. Ding, L. Jiang, W. Guo, *Small* **2019**, *15*, 1804279; d) J. Chen, W. Xin, W. Chen, X. Zhao, Y. Qian, X.-Y. Kong, L. Jiang, L. Wen, *ACS Cent. Sci.* **2021**, *7*, 1486–1492; e) Z. Zhang, S. Yang, P. Zhang, J. Zhang, G. Chen, X. Feng, *Nat. Commun.* **2019**, *10*, 2920; f) J. Xu, S. An, X. Song, Y. Cao, N. Wang, X. Qiu, Y. Zhang, J. Chen, X. Duan, J. Huang, W. Li, Y. Wang, *Adv. Mater.* **2021**, *33*, 2105178.

[6] a) X. He, Y. Yang, H. Wu, G. He, Z. Xu, Y. Kong, L. Cao, B. Shi, Z. Zhang, C. Tongsh, K. Jiao, K. Zhu, Z. Jiang, *Adv. Mater.* **2020**, *32*, 2001284; b) S. Bing, W. Xian, S. Chen, Y. Song, L. Hou, X. Liu, S. Ma, Q. Sun, L. Zhang, *Matter* **2021**, *4*, 2027–2038; c) C. Yuan, X. Wu, R. Gao, X. Han, Y. Liu, Y. Long, Y. Cui, *J. Am. Chem. Soc.* **2019**, *141*, 20187–20197; d) S. Kandambeth, K. Dey, R. Banerjee, *J. Am. Chem. Soc.* **2019**, *141*, 1807–1822; e) D. B. Shinde, G. Sheng, X. Li, M. Ostwal, A.-H. Emwas, K.-W. Huang, Z. Lai, *J. Am. Chem. Soc.* **2018**, *140*, 14342–14349; f) Y. Li, Q. Wu, X. Guo, M. Zhang, B. Chen, G. Wei, X. Li, X. Li, S. Li, L. Ma, *Nat. Commun.* **2020**, *11*, 599; g) J. W. Colson, A. R. Woll, A. Mukherjee, M. P. Levendorf, E. L. Spitler, V. B. Shields, M. G. Spencer, J. Park, W. R. Dichtel, *Science* **2011**, *332*, 228–231; h) Q. Hao, Z.-J. Li, C. Lu, B. Sun, Y.-W. Zhong, L.-J. Wan, D. Wang, *J. Am. Chem. Soc.* **2019**, *141*, 19831–19838; i) F. Sheng, B. Wu, X. Li, T. Xu, M. A. Shehzad, X. Wang, L. Ge, H. Wang, T. Xu, *Adv. Mater.* **2021**, *33*, 2104404; j) Y. Ying, S. B. Peh, H. Yang, Z. Yang, D. Zhao, *Adv. Mater.* **2021**, *33*, 2104946; k) S. Hou, W. Ji, J. Chen, Y. Teng, L. Wen, L. Jiang, *Angew. Chem. Int. Ed.* **2021**, *60*, 9925–9930; *Angew. Chem.* **2021**, *133*, 10013–10018; l) L. Liu, L. Yin, D. Cheng, S. Zhao, H.-Y. Zang, N. Zhang, G. Zhu, *Angew. Chem. Int. Ed.* **2021**, *60*, 14875–14880; *Angew. Chem.* **2021**, *133*, 15001–15006; m) H. Fan, M. Peng, I. Strauss, A. Mundstock, H. Meng, J. Caro, *J. Am. Chem. Soc.* **2020**, *142*, 6872–6877; n) L. Cao, X. Liu, D. B. Shinde, C. Chen, I.-C.

Chen, Z. Li, Z. Zhou, Z. Yang, Y. Han, Z. Lai, *Angew. Chem. Int. Ed.* **2021**, *61*, e202113141; *Angew. Chem.* **2021**, *134*, e202113141; o) S. Zhao, C. Jiang, J. Fan, S. Hong, P. Mei, R. Yao, Y. Liu, S. Zhang, H. Li, H. Zhang, C. Sun, Z. Guo, P. Shao, Y. Zhu, J. Zhang, L. Guo, Y. Ma, J. Zhang, X. Feng, F. Wang, H. Wu, B. Wang, *Nat. Mater.* **2021**, *20*, 1551–1558.

[7] a) L. Hou, W. Xian, S. Bing, Y. Song, Q. Sun, L. Zhang, S. Ma, *Adv. Funct. Mater.* **2021**, *31*, 2009970; b) C. Zhu, W. Xian, Y. Song, X. Zuo, Y. Wang, S. Ma, Q. Sun, *Adv. Funct. Mater.* **2022**, *32*, 2109210.

[8] H. S. Sasmal, A. Halder, H. S. Kunjattu, K. Dey, A. Nadol, T. G. Ajithkumar, P. R. Bedadur, R. Banerjee, *J. Am. Chem. Soc.* **2019**, *141*, 20371–20378.

[9] Q. Sun, Y. Tang, B. Aguila, S. Wang, F.-S. Xiao, P. K. Thallapally, A. M. Al-Enizi, A. Nafady, S. Ma, *Angew. Chem. Int. Ed.* **2019**, *58*, 8670–8675; *Angew. Chem.* **2019**, *131*, 8762–8767.

[10] F. Fornasiero, H. G. Park, J. K. Holt, M. Stadermann, C. P. Grigoropoulos, A. Noy, O. Bakajin, *Proc. Natl. Acad. Sci. USA* **2008**, *105*, 17250–17255.

[11] R. C. Rollings, A. T. Kuan, J. A. Golovchenko, *Nat. Commun.* **2016**, *7*, 11408.

[12] C. Lee, L. Joly, A. Siria, A.-L. Biance, R. Fulcrand, L. Bocquet, *Nano Lett.* **2012**, *12*, 4037–4044.